Nano Research

Open Access

Research Article

Suppressing weak-light voltage attenuation in Sb_2S_3 indoor photovoltaics using Li-doped TiO_2 layer

Kefei Wu[1], Hui Deng[1,2] ✉, Xinxin Feng[1], Jinwei Hong[1], Guidong Wang[1], Muhammad Ishaq[4], Caixia Zhang[1], Qiao Zheng[1], Weihuang Wang[1], Jionghua Wu[1], and Shuying Cheng[1,2,3] ✉

[1] *College of Physics and Information Engineering, Institute of Micro-Nano Devices and Solar Cells, Fuzhou University, Fuzhou 350108, China*
[2] *Fujian Science & Technology Innovation Laboratory for Optoelectronic Information of China, Fuzhou 350108, China*
[3] *Jiangsu Collaborative Innovation Center of Photovoltaic Science and Engineering, Changzhou 213164, China*
[4] *Shenzhen Key Laboratory of Advanced Thin Films and Applications, College of Physics and Optoelectronic Engineering, Shenzhen University, Shenzhen 518060, China*

Cite this article: *Nano Research*, **2025**, *18*, 94907271. https://doi.org/10.26599/NR.2025.94907271

ABSTRACT: Antimony sulfide (Sb_2S_3) thin film have a suitable band gap (1.73 eV) and high absorption coefficient, indicating potential prospects in indoor photovoltaics. The open-circuit voltage (V_{OC}) attenuation under indoor weak light limits the performance and application, which is affected by the heterojunction interface quality. Hence, we propose a hole transport layer free Sb_2S_3 indoor photovoltaic cell using Li-doped TiO_2 as the electron transport layer to overcome weak-light V_{OC} loss. The Li-doped TiO_2 films prepared by spray pyrolysis LiCl additive precursor reveal higher surface potentials, enhancing electron collections. The doped interface also promoted subsequent grain growth of Sb_2S_3 thin film. The champion device, configured as FTO/TiO_2:Li/Sb_2S_3/Au, achieves an efficiency of 6.12% with an optimal Li doping ratio of 8% in the TiO_2 layer. The Li introduction at the junction interface suppresses the photocarrier recombinations under indoor light, thus improving device performance. The indoor power conversion efficiency of the Li-TiO_2 based Sb_2S_3 device reaches 12.7% under the irradiation of 1000-lux LED, showing 48% improvement compared with the undoped device. The Li-doped TiO_2/Sb_2S_3 photovoltaic device demonstrates significant advantages, particularly in cold and monochromatic light conditions, opening new prospects for indoor application.

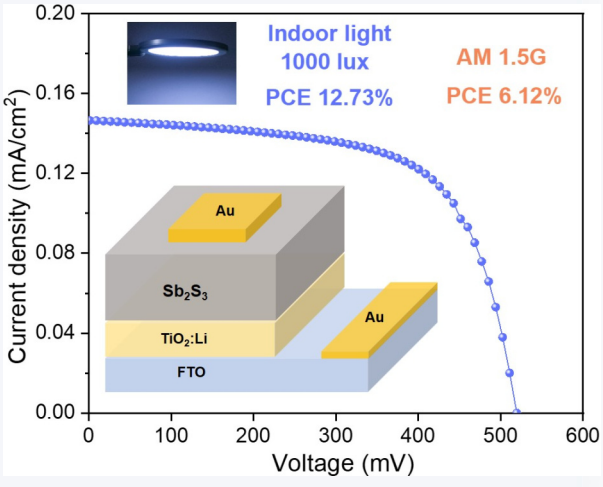

KEYWORDS: Sb_2S_3, indoor photovoltaics, Li-doped TiO_2, V_{OC} improvement, conversion efficiency

1 Introduction

Antimony sulfide (Sb_2S_3) occupies a place in the absorber materials for solar cells [1], which is attributed to its abundant reserves, environmentally friendly properties, and excellent stability both in air and water [2]. Nowadays, with the vigorous development of the internet of things technology (IoT), the demand for energy absorption and reuse continues to expand, bringing indoor photovoltaic applications into the spotlight. According to the theoretical calculations, the theoretical maximum power conversion efficiency (PCE) in the optimal band gap of 1.9 eV can exceed 60% under visible LED light illuminations [3]. Sb_2S_3 exhibits an exceptional absorption coefficient (10^5 cm^{-1}) within the visible light range of 450–600 nm. Simultaneously, the 1.73 eV band gap of the Sb_2S_3 solar cell aligns perfectly with the optimal band gap value, establishing it as an ideal candidate for indoor photovoltaic applications [4].

In Sb_2S_3 photovoltaic devices, the interfacial barriers, lattice mismatch, intrinsic defects, and orientations are critical issues to affect device performance, especially in weak-light indoor conditions [5]. The study on process optimization [6], device structure [7], and defect passivation [8] of the Sb_2S_3 solar cells achieved significant advancements [9–11]. The primary methods

Received: December 23, 2024; **Revised:** January 17, 2025
Accepted: January 22, 2025

✉Address correspondence to Hui Deng, denghui@fzu.edu.cn; Shuying Cheng, sycheng@fzu.edu.cn

employed for the fabrication of Sb_2S_3 photovoltaic devices are chemical water bath deposition (CBD) [12], rapid thermal evaporation (RTE) [13, 14], vapor transport deposition (VTD) [15], and hydrothermal method (HT) [16]. The Sb_2S_3 photovoltaic cells based on the solution method have achieved high performance. Seok et al. conducted surface vulcanization treatment on the Sb_2S_3 film using thioacetamide (TA) treatment, resulting in a PCE of 7.5%. Wang et al. reported 8.32%-efficiency Sb_2S_3 solar cells prepared through the CBD method [12]. In the device structure, organic hole transport layers (HTL) such as spiro-OMeTAD and P3HT face application bottlenecks related to cost and stability [17]. Nevertheless, the vacuum method for Sb_2S_3 enables the straightforward construction of HTL free full-inorganic photovoltaic devices [18]. The performances of the vacuum-based HTL free photovoltaic devices still fall short of the requirements for commercialization. Interestingly, wide band-gap Sb_2S_3 photovoltaic cells, which are well-matched to the entire visible spectrum, can be further developed to enhance device performance for indoor applications.

Indoor photovoltaic cells serve as crucial carriers of energy and information, playing a vital role in the development of smart cities that prioritize non-toxicity and stability [19]. Sb_2S_3 photovoltaic cells based on titanium oxide (TiO_2) as an electron transport layer (ETL) meet indoor requirements [20]. It has been reported that solar cell performance, particularly open circuit voltage (V_{OC}) and short circuit current (J_{SC}), experiences significant degradation under weak light conditions due to insufficient charge extraction and separation. The low conductivity of TiO_2 is attributed to the presence of oxygen vacancies, and the observed energy level shift indicates a lower conduction band in TiO_2 compared to that of the Sb_2S_3 absorption layer [21, 22]. Consequently, this results in decreased electron flow from the Sb_2S_3 layer, hindering the efficient transfer of photogenerated charge carriers at the interface. Doping emerges as a crucial approach for modifying lattice vacancies and Fermi levels, thereby addressing this issue and enhancing electron extraction [23]. A Ru-doped TiO_2 compact layer was used in dye-sensitized solar cells, serving as a blocking layer to reduce charge recombination [24]. The conductivity and surface morphology of the TiO_2 film can be enhanced by doping Al, Cs, and Y to improve the performance of perovskite solar cells [25]. Meanwhile, the study of Zn-doped TiO_2 film indicated the enhancement of the V_{OC} for Sb_2S_3 solar cells [26]. Thus, doping for TiO_2 ETL is an efficient strategy to improve heterojunction quality and regulate voltage attenuation.

In this work, the Sb_2S_3 thin film photovoltaic device in the configuration of FTO/TiO_2:Li/Sb_2S_3/Au is developed for indoor applications. To mitigate the V_{OC} attenuation under weak light, the Li^+ ions are incorporated into the TiO_2 layer employing a precursor solution with lithium chloride (LiCl). The influences of Li doping concentration on devices are investigated by material characterization and electrical property measurements. The Li doping TiO_2 layer significantly enhances the V_{OC} and PCE of the device. The optimized Sb_2S_3 photovoltaic cell obtains 6.12% efficiency in a standard sunlight (AM 1.5G). Moreover, under the illumination of LED (1000 lux), the device exhibits PCEs of 11.3% and 12.7% in warm and cold light, respectively.

2 Results and discussion

The spray pyrolysis method offers several advantages for the preparation of TiO_2 films, including low cost, convenient adjustment of film thickness, and doping capability. The ion doping helps to enhance the conductivity of TiO_2 ETL and suppress interfacial defects to overcome weak-light V_{OC} attenuation of the Sb_2S_3 photovoltaic devices [27]. Figure 1(a) illustrates the schematic diagram depicting the process of TiO_2 preparation through spray pyrolysis. The LiCl serves as the source material to achieve Li doping in the TiO_2 films. The LiCl is solid powder at room temperature, inexpensive, and easily soluble in the precursor solution of TiO_2, enabling precise control over doping levels. The Sb_2S_3 thin film is deposited on the Li-doped TiO_2 film using the RTE method to fabricate the HTL-free photovoltaic cell in the configuration of FTO/TiO_2:Li/Sb_2S_3/Au, as illustrated in Fig. 1(b). The absorption spectrum of the Sb_2S_3 film is shown in Fig. 1(c), which ranges from 360 to 720 nm and covers visible wavelengths. As shown in Fig. 1(d), according to the reported research and calculations, the theoretical maximum efficiency of the Sb_2S_3 photovoltaic cell under the AM 1.5G is 26% [28, 29]. However, under LED irradiation conditions, the theoretical maximum efficiency is more than 50%, which is attributed to its wide band gap (1.73 eV) [30, 31]. This positions Sb_2S_3 as an ideal material for indoor photovoltaics, efficiently absorbing indoor lights.

The compositions of Li doping of TiO_2 films are investigated by X-ray photoelectron spectroscopy (XPS). The binding energy has been calibrated concerning the carbon signals. The typical peaks arising from TiO_2 films (Ti 2p, Ti 2s, Ti 3p, O 1s) [32] are readily apparent (Fig. S1 in the Electronic Supplementary Material (ESM)). High-resolution characteristic spectra of Ti 2p, O 1s and Li 1s lines probed for the undoped and Li-doped TiO_2 film are shown in Figs. 2(a)–2(c), respectively. The Ti 2p peaks at 464.1 and 458.5 eV (Fig. 2(a)), the Ti–O peak at 529.7 eV and the O–H peak at 531.8 eV (Fig. 2(b)) are well matched with the standard peak positions of TiO_2 [33, 34]. Ti and O reveal a good combination with an atomic ratio of 1:1.9. As shown in Fig. 2(c), the peak of 57.1 eV represents the Li signal detected for Li-doped TiO_2 film [35]. The main peak positions of Ti and O remain unchanged after Li doping, which does not destroy the chemical bonds and crystal lattices. Because of the small atomic radius of Li, it undergoes interstitial doping in TiO_2 [36]. At the same time, the Li doping boosts the conductivity of TiO_2 from 1.57×10^{-7} to 1.09×10^{-6} S/cm (Fig. S2 in the ESM). The surface morphology and roughness of undoped and Li-doped TiO_2 films are characterized by scanning electron microscope (SEM) and atomic force microscope (AFM). As shown in Figs. 2(d) and 2(g), the surface roughness of the undoped and Li-doped TiO_2 films are 38.6 and 36.2 nm, respectively. Both the two TiO_2 films have compact surfaces composed of large grains (Fig. S3 in the ESM). The Li doping does not significantly affect the morphology or roughness. Subsequently, surface potentials and charge distributions of the TiO_2 film are further investigated by Kelvin probe force microscopy (KPFM). Obviously, Li doping causes a significant change in the surface potential of the TiO_2 film, revealing overall improvement and more uniform distribution (Figs. 2(e) and 2(h)). The extracted surface height and potential values of the control and Li-doped TiO_2 films are illustrated in Figs. 2(f) and 2(i). The surface potential of undoped TiO_2 films ranges from −4 to 4 mV, while Li-doping increases it to approximately 120 mV. Furthermore, the higher surface potentials and conductivity from Li doping indicate lower work function and stronger electronic collection ability of TiO_2 ETL.

To evaluate the effect of Li doping (0%, 4%, 6%, 8%, 10%, and 12% (Li/(Li+Ti)) in TiO_2 on the post-deposited Sb_2S_3 layer, the

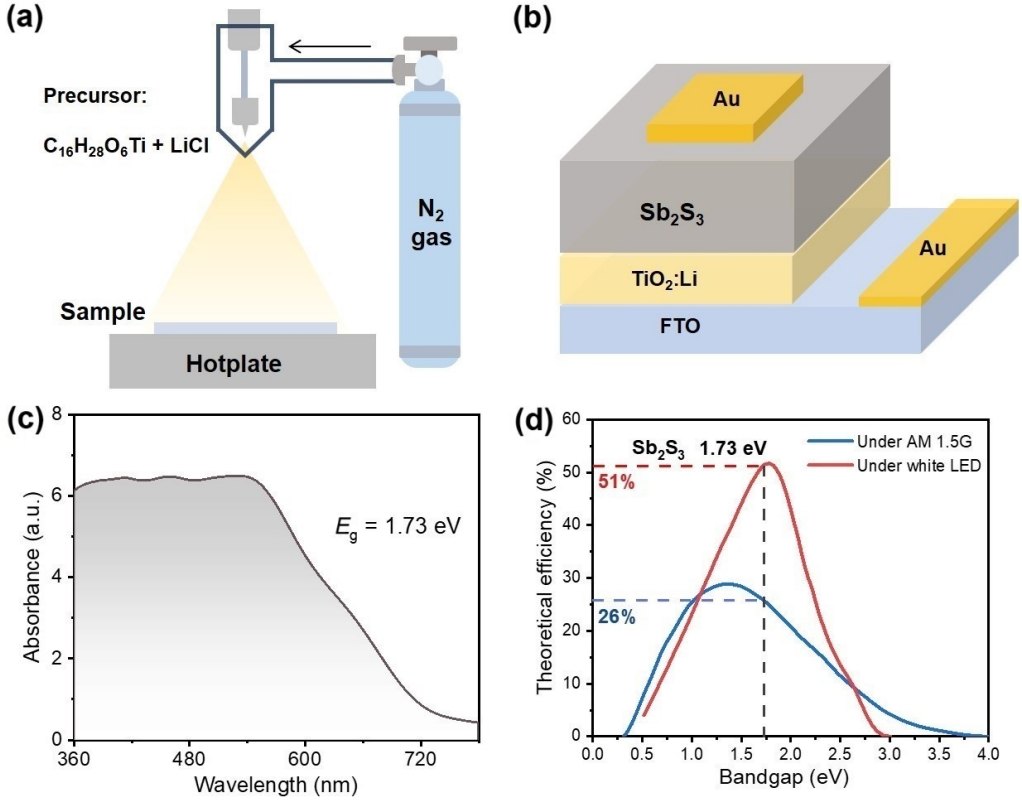

Figure 1 (a) Schematic diagram of spray pyrolysis. (b) Device structure of Li-doped ETL Sb_2S_3 photovoltaic cells. (c) UV–vis absorption spectrum of the Sb_2S_3 film. (d) Theoretical SQ limit at various values of E_g.

surface morphologies of Sb_2S_3 thin films are studied via SEM, as depicted in Figs. 3(a)–3(f), respectively. Obviously, the Li doping in TiO_2 enhances the crystallization of the Sb_2S_3 films. On the 8% Li-doped TiO_2, the Sb_2S_3 crystals exhibit optimal fullness and density while maintaining a flat film surface with minimal voids. Additionally, the average grain size is approximately 500 nm by measurement. Large and densely packed grains are advantageous in reducing grain boundary scattering and facilitating carrier migration. However, when the doping ratio reaches 12%, the quality of the Sb_2S_3 film decreases significantly. Excessive doping of Li results in the precipitation of numerous particles on the surface of TiO_2 film during annealing, which compromises the quality of heterojunction and ultimately impedes the growth of the Sb_2S_3 film. Figures 3(g) and 3(h) depict the SEM cross-section images of Sb_2S_3/TiO_2 films doped with ratios of 0% and 8%. It can be observed that the TiO_2 and Sb_2S_3 films exhibit distinct demarcations. The thickness of the TiO_2 film is about 50 nm, and the Sb_2S_3 film is about 450 nm. Under identical deposition conditions, Li-doped TiO_2 facilitates the growth of the Sb_2S_3 film. In addition, the X-ray diffraction (XRD) measurement (Fig. S4 in the ESM) indicates that Li-doped TiO_2 enhances diffraction peaks at crystal directions (110), (120), and (220) of the Sb_2S_3 film to improve crystal quality.

The effects of Li-doped concentrations for TiO_2 on the performance of Sb_2S_3 photovoltaic devices are investigated. Figs. 4(a)–4(d) present statistical performance indicators including V_{OC}, J_{SC}, fill factor (FF), and PCE. With the increases in Li doping ratio from 0% to 8% (Li/(Li+Ti)), V_{OC}, J_{SC}, and PCE exhibit significant enhancements. The 8%-Li doping ratio for TiO_2 film realizes optimal performance. When the doping ratio exceeds 8%, the performances show a downward trend. Moreover, the device with a doping ratio of 12% demonstrates a sharp decline in performance. Excessive doping damages the lattice of TiO_2 and heterojunction interface, causing serious V_{OC} loss. The current density vs. voltage (J–V) curves of the four devices are shown in Fig. 4(e). The PCE of the control Sb_2S_3 solar cell without Li doping is 5.03% with a V_{OC} of 645 mV. Notably, the Sb_2S_3 device with an 8% Li doping ratio in TiO_2 achieves a PCE of 6.12%, a V_{OC} of 713 mV, a J_{SC} of 17.04 mA/cm^2, and an FF of 50.3%. The Li-doped TiO_2 ETL leads to a 12% and 20% improvement in the V_{OC} and PCE, respectively. The external quantum efficiency (EQE) spectrum with varying doping densities is shown in Fig. 4(f). The doping density in TiO_2 enables higher EQE across the full spectrum range, enhancing the J_{SC}. The EQE of the Sb_2S_3 device with the 8% Li-doped TiO_2 is beyond 80% at the wavelengths of 400–550 nm, manifesting superior light absorption and utilization capabilities within indoor visible light.

The quality factor (A) and reverse saturation current density (J_0) are important parameters for the PN junction, which can be determined from the dark J–V curves in Fig. 5(a). Compared to the undoped TiO_2 device (3.17×10^{-5} mA/cm^2), the Li-doped TiO_2 device exhibits a smaller J_0 (1.31×10^{-5} mA/cm^2), indicating faster carrier transmission and reduced charge recombination due to doping. In addition, the A of the Li-doped TiO_2 device decreases from 1.91 to 1.78, confirming an enhancement in PN junction quality. The charge recombination lifetime (τ_r) and transfer lifetime (τ_t) are important parameters for analyzing the charge states, which can be characterized by time-resolved transient photovoltage (TPV)

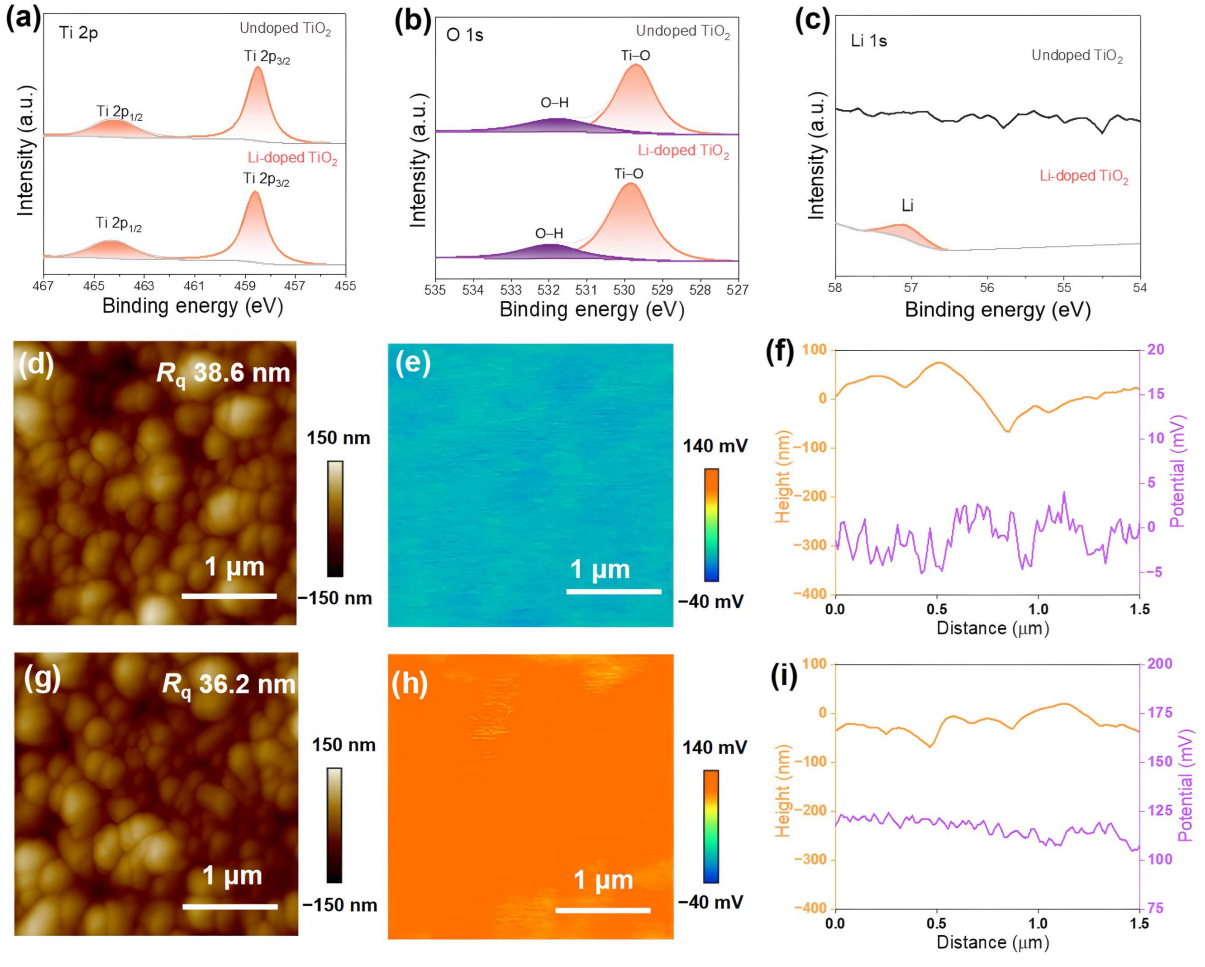

Figure 2 XPS spectra of (a) Ti 2p, (b) O 1s and (c) Li 1s for undoped TiO_2 and Li-doped TiO_2. AFM surface roughness images of (d) undoped TiO_2 film and (g) Li-doped TiO_2 film. KPFM results (CPD) for the samples of (e) undoped TiO_2 film and (h) Li-doped TiO_2 film. Surface potential trend diagram of (f) undoped TiO_2 film and (i) Li-doped TiO_2 film (the orange color shows the contact current difference, whereas the height is represented by purple color).

and transient photocurrent (TPC). As shown in Fig. 5(b), the Li-doped TiO_2 device exhibits a higher τ_r value of 164 μs from TPV decay under open circuit conditions compared to the undoped TiO_2 device with a τ_r value of 96.3 μs. This indicates that the recombination of photocarriers is better suppressed in the PN junction. In Fig. 5(c), the calculated τ_t values from TPC decay under short-circuit conditions for the undoped and Li-doped TiO_2 devices are 8.22 and 5.25 μs, respectively. Therefore, the Li doping of the TiO_2 film effectively passivates defects in the PN junction to suppress recombination and enhance charge transfer. The carrier recombination characteristics in photovoltaic devices can be analyzed using electrochemical impedance spectroscopy (EIS), where the abrupt PN heterojunction capacitance can be approximated using a parallel-plate capacitor model with an equivalent circuit diagram (Fig. 5(d)). The recombination resistances (R_{rec}) of the undoped and Li-doped TiO_2 devices are 6.4 and 15.2 kΩ, respectively. The higher R_{rec} values indicate positive effects on carrier separation and transport. The V_{OC} and J_{SC} characteristics dependent on the intensity of light (I_{light}) are investigated to analyze the recombination mechanism in the devices. Figure 5(e) illustrates the light-dependent V_{OC} for the two devices. In a trap-free photovoltaic device, a specific value (n) of 1 is observed between the slope of V_{OC} versus $\ln(I_{light})$ and (kT/q). For undoped TiO_2 and Li-doped TiO_2 devices, n values of 1.34 and 1.21 are obtained respectively, indicating reduced trap-assisted recombination in alkali metal-doped devices. Figure 5(f) demonstrates a power law relationship between J_{SC} and I_{light} ($J_{SC} \propto I_{light}^{\alpha}$) for the devices [37]. The α values for undoped TiO_2 and Li-doped TiO_2 devices are found to be 0.973 and 0.986 respectively, suggesting that trap-assisted recombination dominates in these devices. Furthermore, a larger α value reveals an enhanced carrier extraction capability in Li-doped TiO_2 device [38]. Based on the above the performance degradation of Sb_2S_3 devices in weak light environments is expected to be mitigated by Li-doped TiO_2.

The Sb_2S_3 photovoltaic devices are irradiated by two kinds of LED lights to investigate indoor photovoltaic performance. Figure 6(a) illustrates the spectral composition of different color temperature modes of the LED lamp used at an illuminance level of 1000 lux. The cold light with around 6000 K of temperature is mainly blue, while warm light with a temperature of 3000 K is primarily orange [39]. The wavelength of common indoor light sources ranges from 420–720 nm, which aligns perfectly with the absorption range of the Sb_2S_3 absorption layer. This indicates that Sb_2S_3 can effectively cover the entire indoor spectra, making it highly suitable for indoor photovoltaic applications. Figures 6(b)–6(e) present variations in photovoltaic performance for device groups with Li-doped TiO_2 under different LED light intensities. And the related photovoltaic parameters are listed in

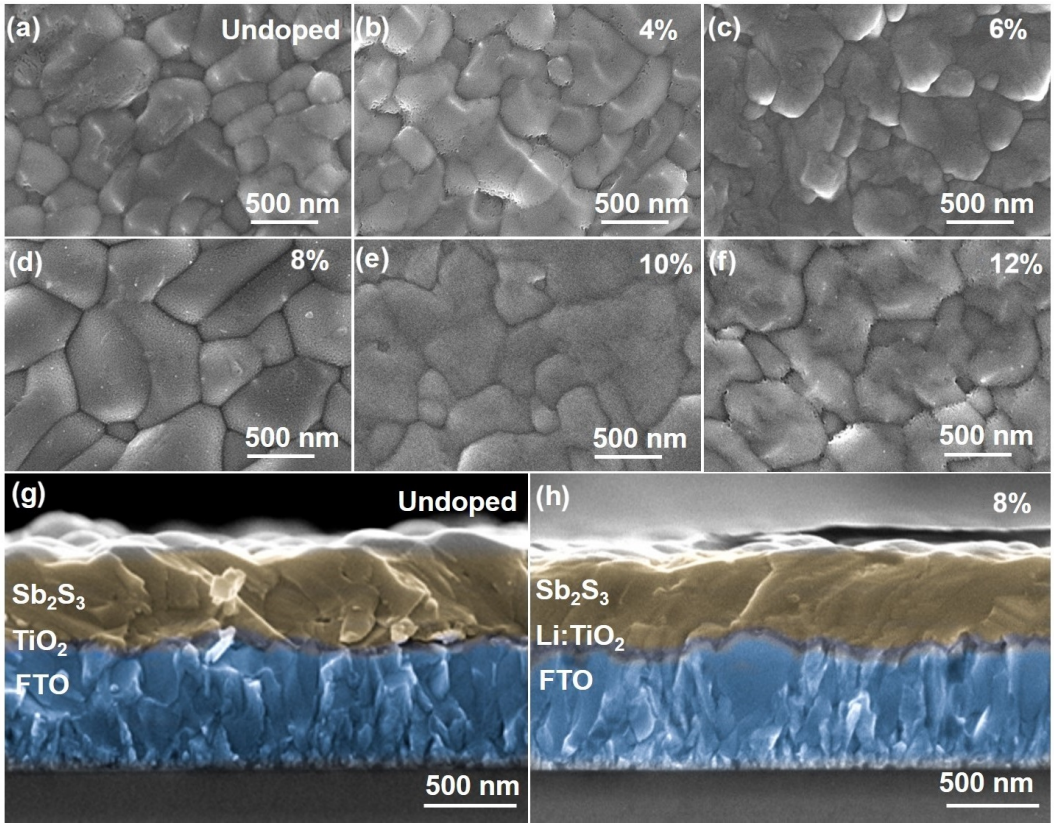

Figure 3 Top-view SEM images of the Sb_2S_3 films grown on TiO_2 layers with different Li doping ratios (Li/Ti): (a) undoped, (b) 4%, (c) 6%, (d) 8%, (e) 10%, and (f) 12%. Cross-section SEM images of the Sb_2S_3 films grown on TiO_2 layers with (g) undoped and (h) 8% doping ratios.

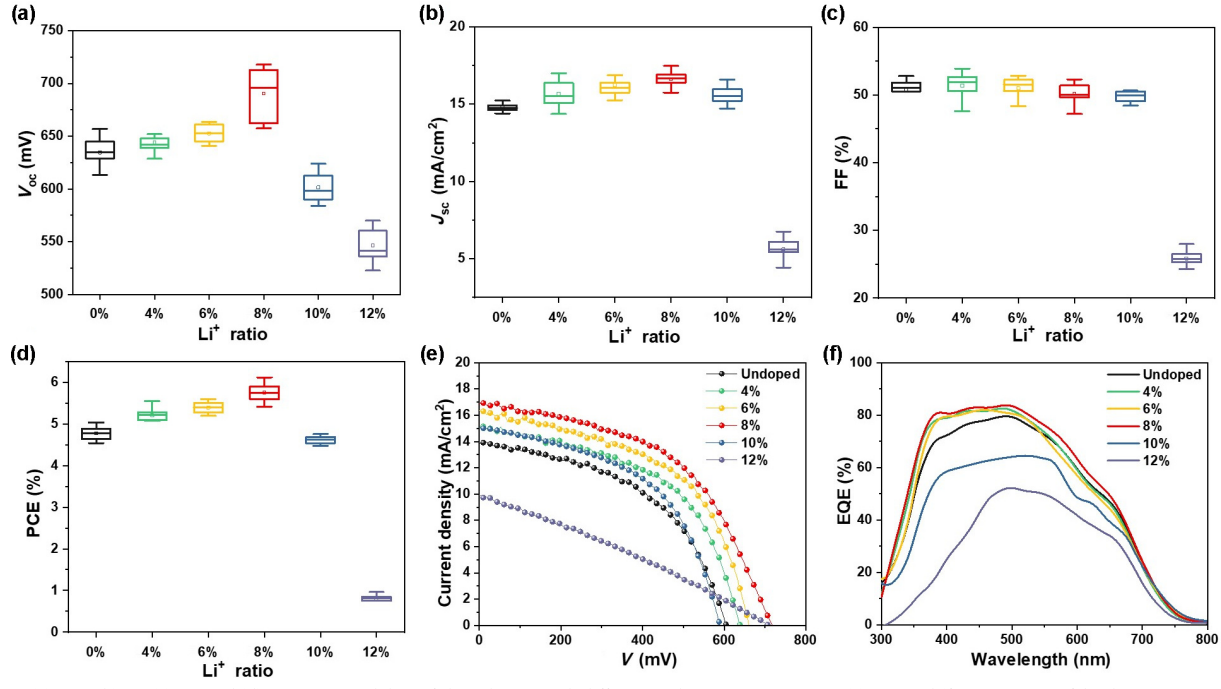

Figure 4 (a) V_{OC}, (b) J_{SC}, (c) FF, and (d) PCE statistical data of Sb_2S_3 devices with different Li doping ratios in TiO_2. (e) *J*–*V* and (f) EQE curves of the devices.

Table 1. The photovoltaic performance is enhanced under the two LED lamps, resulting in a significant increase in overall performance. The V_{OC} attenuation is effectively suppressed at light intensities below 500 lux (Fig. 6(b)). Meanwhile, the device maintains an FF of above 52% (Fig. 6(c)). Both groups of devices show an increase in J_{SC} under cold light conditions due to better spectral matching between Sb_2S_3 and cold light (Fig. 6(d)). As shown in Figs. 6(e) and 6(f), the champion device achieves a PCE of 12.7% at 1000 lux, which is improved by 48% compared with the undoped group (8.6%). Consequently, the HTL-free Sb_2S_3 indoor

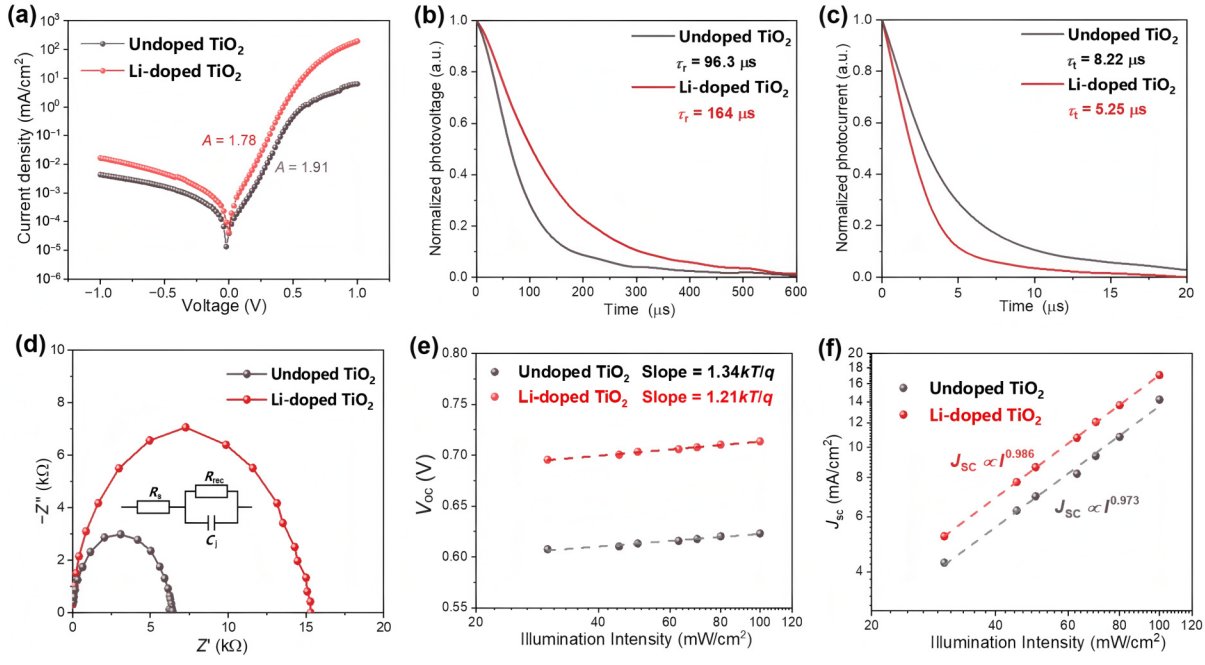

Figure 5 (a) Dark *J*–*V* curves, (b) TPV decay, (c) TPC decay, and (d) EIS analysis of the two devices. (e) The V_{OC} and (f) J_{SC} versus light intensity plots.

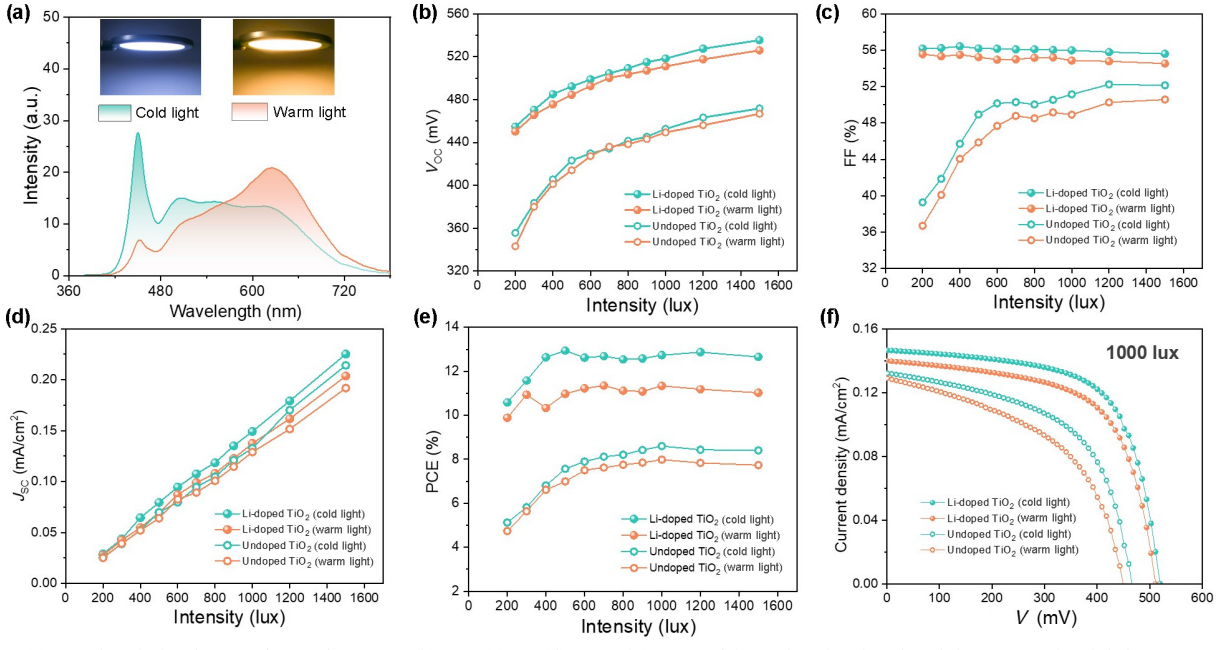

Figure 6 (a) Wavelength distribution of LEDs for testing. (b) V_{OC}, (c) FF, (d) J_{SC}, and (e) PCE of the undoped and Li-doped devices varied with light intensity. (f) *J*–*V* performance of the two devices under 1000 lux cold and warm light illuminations.

Table 1 Photovoltaic parameters of the control and optimal doping concentration devices under different illumination conditions

Light	Device group	V_{OC} (mV)	J_{SC} (mA/cm²)	FF (%)	PCE (%)
AM 1.5 G	Undoped TiO_2	645	15.44	50.54	5.03
	8%-Li-doped TiO_2	713	17.04	50.28	6.12
LED 1000 lux (warm light)	Undoped TiO_2	449	0.129	48.91	7.98
	8%-Li-doped TiO_2	511	0.137	54.86	11.30
LED 1000 lux (cold light)	Undoped TiO_2	452	0.133	51.15	8.60
	8%-Li-doped TiO_2	518	0.149	55.99	12.73

photovoltaic cells exhibit superior performance in cold light environments.

Monochromatic light is commonly observed in various indoor settings, such as interior decoration. The four typical monochromatic light sources in the experiment are shown in Fig. 7(a), which are blue (400 nm), green (530 nm), bright red (625 nm), and deep red (700 nm). An optical power densitometer calibrates the irradiances of all the light sources to 0.5 mW/cm². The resulting PCE is presented in Fig. 7(b). Following Li doping in the TiO_2 ETL, the device exhibits enhanced responses to four different monochromatic lights. The PCEs of the photovoltaic device are

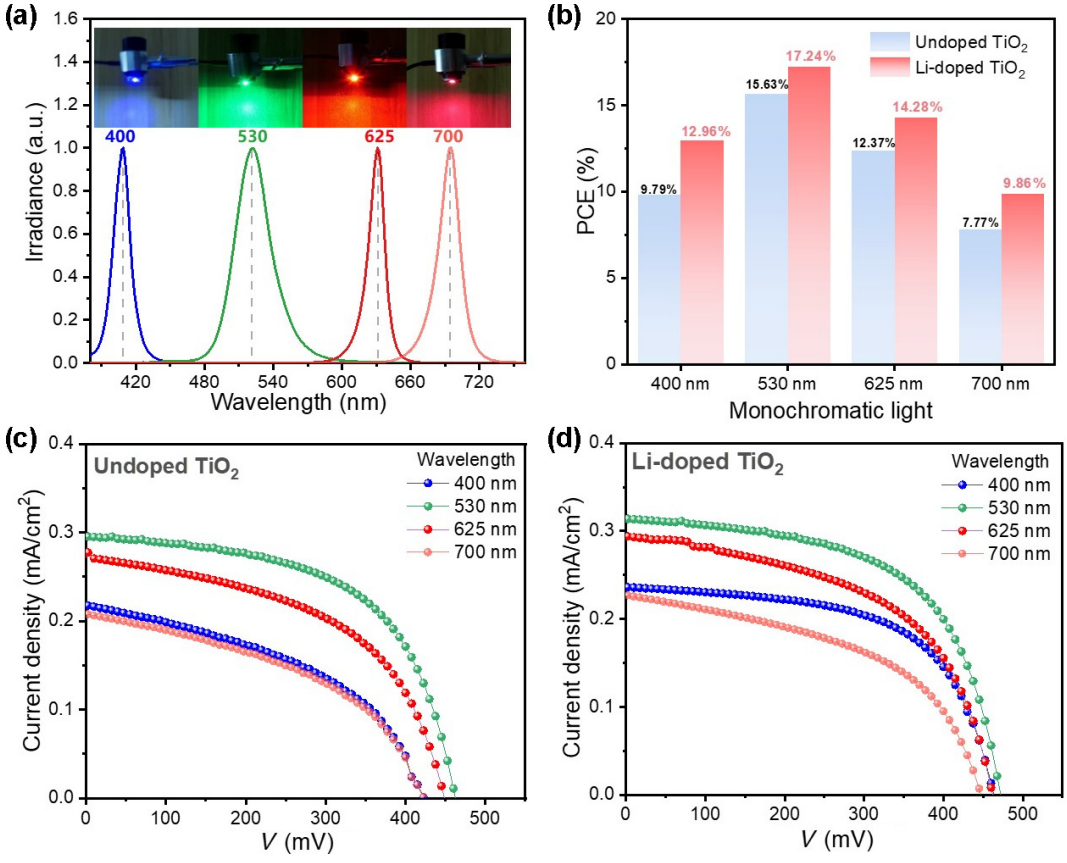

Figure 7 (a) Common monochromatic light sources for testing. (b) Performance comparison under monochromatic lights with the irradiation of 0.5 mW/cm^2. (c) and (d) *J*–*V* curves under monochromatic lights with the 0.5 mW/cm^2 irradiation.

12.96%, 17.24%, 14.28%, and 9.86% under illuminations of blue, green, bright red, and deep red, respectively. All the curves with rectification effects reveal a good response to weak light. The performance of the Li-doped TiO_2 device under red light realizes a large improvement by more than 30%. Among them, the response to green light is the strongest, with an achieved FF of more than 60%. Therefore, the Li-doped TiO_2 device has obtained significant improvement in performance in monochromatic light, thus indicating it is highly suitable for applications in the indoor monochromatic light environment.

3 Conclusion

In summary, we propose an HTL-free full-inorganic Sb_2S_3 indoor photovoltaic cell in a configuration of FTO/TiO_2:Li/Sb_2S_3/Au using Li-doped TiO_2 ETL to overcome weak-light V_{OC} loss. The Li-doped TiO_2 films prepared using spray pyrolysis, exhibit higher surface potentials that enhance electron collection. Additionally, Li doping promotes the growth of Sb_2S_3 grains, resulting in a high-quality heterojunction of TiO_2/Sb_2S_3. The PCE of all inorganic Sb_2S_3 photovoltaic devices based on Li-doped TiO_2 under AM 1.5G has reached 6.12%, with a V_{OC} of 713 mV, a J_{SC} of 17.04 mA/cm^2, and an FF of 50.3%. The Li-doped TiO_2 layer increases device recombination resistance from 6.4 to 15.2 kΩ while exhibiting a short charge transfer lifetime of 5.25 μs and a long recombination lifetime of 164 μs, indicating excellent charge extraction and transport effects. Notably, the champion device achieves a PCE of 12.7% at 1000 lux, indicating a 48% improvement over the undoped sample (8.6%). It maintains a high V_{OC} and FF even under indoor weak light conditions due to the inhibited carrier recombination loss. Additionally, the device exhibits excellent response to monochromatic light sources, particularly green light, achieving a PCE of 17.24%.

4 Methods

4.1 Device fabrication.

The FTO conductive glasses (2.5 cm × 2.5 cm) as substrates were conducted by ultrasonic cleaning. The TiO_2 precursor solution was prepared by mixing titanium diisopropoxide bis(acetylacetonate) (75 wt.% isopropanol, Sigma) with absolute ethyl alcohol in a volume ratio of 1:9 and stirred for over 48 h. The Li-doped TiO_2 films were prepared by controlling the precursor. The lithium chloride (LiCl) powder (99%, Aladdin Industrial Corporation) was added to the precursor solution at quantities of 0.088, 0.176, and 0.352 g per 10 mL of solution to obtain different doping concentrations. The TiO_2 precursor solutions were sprayed onto the FTO substrates using N_2 gas at a temperature of 450 °C followed by annealing at 560 °C for 30 min. The Sb_2S_3 films were deposited by the RTE method. The 0.4 g Sb_2S_3 powder (98%, Aladdin Industrial Corporation) was used as the evaporation source. The RTE vacuum equipment (OTF-1200X) which was equipped with a covered graphite block, maintained the sample temperature at 300 °C for 15 min. Then, the temperature was increased from 300 to 560 °C within 15 sand remained constant for another 40 s. The vacuum level was maintained below 4 × 10^{-3} Torr in the evaporation process. After cooling to room temperature, the compact Sb_2S_3

films were obtained. The gold electrodes (device area, 0.04 cm^2) were fabricated by thermal evaporation, constructing the device in the configuration of FTO/TiO_2:Li/Sb_2S_3/Au.

4.2 Characterizations and measurements.

The surface and cross-sectional morphologies of the devices were analyzed using a Dual Beam FEG SEM (Helios G4 CX) equipped with a focused ion beam (FIB) technique. The XRD patterns were measured using a Rigaku SmartLab instrument (Cu Kα radiation, 40 kV, 30 mA) within the range of 10° to 60° at a scan rate of 10 °/min. The absorption spectrum of the device was measured in the wavelength range of 300–800 nm using an Agilent CARY5000 spectrophotometer. Surface states were characterized by XPS analysis using an ESCALAB 250 instrument. All XPS binding energies were calibrated based on the C contamination peak at 284.8 eV in the C1s spectrum. Surface roughness and potential profile analyses were conducted using a Bruker Dimension Icon with an MESP probe operating at a frequency of 1 Hz. A power meter (Keithley 2400) and a solar simulator (SUN 2000, ABET) with a power density of 100 mW/cm^2 were used to measure the current density voltage (*J*–*V*) curve of the device. The external quantum efficiency (EQE) spectra were tested by the QE system (Zolix SCS100, CROWNTECH). The dark state current–voltage curves were performed using a semiconductor characterization system (Keithley 4200-SCS, USA) at a frequency of 50 kHz and a DC bias voltage of −1 to 1 V. Electrochemical impedance spectroscopy (EIS) was measured using an electrochemical workstation (VPS) in the frequency range of 1 Hz to 1 MHz under unbiased voltage.

Electronic Supplementary Material: Supplementary material (XPS patterns, *I*–*V* curve and top-view SEM images of TiO_2 films and XRD patterns of Sb_2S_3 films) is available in the online version of this article at https://doi.org/10.26599/NR.2025.94907271.

Data availability

All data needed to support the conclusions in the paper are presented in the manuscript and the ESM. Additional data related to this paper may be requested from the corresponding author upon request.

Acknowledgments

This work is supported by the National Natural Science Foundation of China (Nos. 52372183, 62474043 and 52002073), Fujian Provincial Natural Science Foundation of China (No. 2024J09015), Fujian Science & Technology Innovation Laboratory for Optoelectronic Information of China (No. 2021ZZ124), Foundation of Fujian Provincial Department of Industry and Information Technology of China (No. 82318075), and Fuzhou University (No. XRC-24072).

Declaration of competing interest

All the contributing authors report no conflict of interests in this work.

Author contribution statement

K. F. W.: Investigation, data curation, validation, writing manuscript, experimental design. H. D.: Project administration, funding acquisition, experimental design, supervision, writing manuscript. X. X. F.: Investigation, validation. J. W. H.: Investigation, validation. G. D. W.: Formal analysis. M. I.: Investigation, validation, writing – review & editing. C. X. Z.: Validation, data curation. Q. Z.: Validation, data curation. W. H. W.: Validation, data curation, experimental design. J. H. W.: Data curation, formal analysis. S. Y. C.: Project administration, funding acquisition, supervision. All the authors have approved the final manuscript.

Use of AI statement

None.

References

[1] Chen, J. W.; Li, G. Y.; Xu, Z. H.; Xu, C. C.; Naveed, F.; Liu, B.; Zhang, Y.; Zhou, R.; Chen, C.; Wang, M. T. et al. Recent advances and prospects of solution-processed efficient Sb_2S_3 solar cells. *Adv. Funct. Mater.* **2024**, *34*, 2313676.

[2] Wang, X. M.; Tang, R. F.; Wu, C. Y.; Zhu, C. F.; Chen, T. Development of antimony sulfide-selenide $Sb_2(S, Se)_3$-based solar cells. *J. Energy Chem.* **2018**, *27*, 713–721.

[3] Venkateswararao, A.; Ho, J. K. W.; So, S. K.; Liu, S. W.; Wong, K. T. Device characteristics and material developments of indoor photovoltaic devices. *Mater. Sci. Eng. R: Rep.* **2020**, *139*, 100517.

[4] Chen, X.; Shu, X. X.; Zhou, J. C.; Wan, L.; Xiao, P.; Fu, Y. C.; Ye, J. Z.; Huang, Y. T.; Yan, B.; Xue, D. J. et al. Additive engineering for Sb_2S_3 indoor photovoltaics with efficiency exceeding 17%. *Light: Sci. Appl.* **2024**, *13*, 281.

[5] Saha, A.; Haque, K. A.; Baten, M. Z. Performance evaluation of single-junction indoor photovoltaic devices for different absorber bandgaps under spectrally varying white light-emitting diodes. *IEEE J. Photovolt.* **2020**, *10*, 539–545.

[6] Guo, H. F.; Huang, S.; Zhu, H.; Zhang, T. Y.; Geng, K. J.; Jiang, S.; Gu, D.; Su, J.; Lu, X. L.; Zhang, H. et al. Enhancement in the efficiency of Sb_2Se_3 solar cells by triple function of lithium hydroxide modified at the back contact interface. *Adv. Sci.* **2023**, *10*, 2304246.

[7] Yang, J. J.; Wang, H. L.; Che, B.; Huang, L.; Gao, J. X.; Cai, Z. Y.; Zhu, C. F.; Tang, R. F.; Chen, T. Manipulating the intrinsic defect of MnS by surface sulfidation for inverted $Sb_2(S,Se)_3$ planar-heterojunction solar cells. *Solar RRL* **2024**, *8*, 2400006.

[8] Mo, A. M.; Feng, Y.; Yang, B. X.; Dang, W.; Liang, X. Y.; Cao, W. J.; Guo, Y. N.; Chen, T.; Li, Z. Q. Controlling unintentional defects enables high-efficient antimony selenide solar cells. *Adv. Funct. Mater.* **2024**, *34*, 2316292.

[9] Li, K.; Cai, Z. Y.; Yang, J. J.; Wang, H. L.; Zhang, L. J.; Tang, R. F.; Zhu, C. F.; Chen, T. Molecular beam epitaxy deposition of *in situ* O-doped CdS films for highly efficient $Sb_2(S,Se)_3$ solar cells. *Adv. Funct. Mater.* **2023**, *33*, 2304141.

[10] Lin, J. H.; Mahmood, A.; Chen, G. J.; Ahmad, N.; Chen, M. D.; Fan, P.; Chen, S.; Tang, R.; Liang, G. X. Crystallographic orientation control and defect passivation for high-efficient antimony selenide thin-film solar cells. *Mater. Today Phys.* **2022**, *27*, 100772.

[11] Lin, J. H.; Chen, G. J.; Ahmad, N.; Ishaq, M.; Chen, S.; Su, Z. H.; Fan, P.; Zhang, X. H.; Zhang, Y.; Liang, G. X. Back contact interfacial modification mechanism in highly-efficient antimony selenide thin-film solar cells. *J Energy Chem* **2023**, *80*, 256–264.

[12] Wang, S. Y.; Zhao, Y. Q.; Che, B.; Li, C.; Chen, X. L.; Tang, R. F.; Gong, J. B.; Wang, X. M.; Chen, G. L.; Chen, T. et al. A novel multi-sulfur source collaborative chemical bath deposition technology enables 8%-efficiency Sb_2S_3 planar solar cells. *Adv. Mater.* **2022**, *34*, 2206242.

[13] Deng, H.; Chen, S. W.; Ishaq, M.; Cheng, Y. S.; Sun, Q. Z.; Lin, X.; Zheng, Q.; Zhang, C. X.; Cheng, S. Y. Efficient all-inorganic Sb_2S_3 solar cells with matched energy levels using Sb_2Se_3 as hole transport layers. *Solar RRL* **2022**, *6*, 2101017.

[14] Deng, H.; Zeng, Y. Y.; Ishaq, M.; Yuan, S. J.; Zhang, H.; Yang, X. K.; Hou, M. M.; Farooq, U.; Huang, J. L.; Sun, K. W. et al. Quasiepitaxy strategy for efficient full-inorganic Sb_2S_3 solar cells. *Adv. Funct. Mater.* **2019**, *29*, 1901720.

[15] Li, K. H.; Lu, Y.; Ke, X. X.; Li, S.; Lu, S. C.; Wang, C.; Wang, S. Y.; Chen, C.; Tang, J. Over 7% efficiency of $Sb_2(S,Se)_3$ solar cells via V-shaped bandgap engineering. *Solar RRL* **2020**, *4*, 2000220.

[16] Zhang, L. J.; Lian, W. T.; Zhao, X. C.; Yin, Y. W.; Chen, T.; Zhu, C. F. Sb_2S_3 seed-mediated growth of low-defect Sb_2S_3 on a TiO_2 substrate for efficient solar cells. *ACS Appl. Energy Mater.* **2020**, *3*, 12417–12422.

[17] Liu, X. N.; Cai, Z. Y.; Wan, L.; Xiao, P.; Che, B.; Yang, J. J.; Niu, H. H.; Wang, H.; Zhu, J.; Huang, Y. T. et al. Grain engineering of Sb_2S_3 thin films to enable efficient planar solar cells with high open-circuit voltage. *Adv. Mater.* **2024**, *36*, 2305841.

[18] Li, H.; Yang, G. Q.; Hu, X. Y.; Hu, Y. H.; Zeng, R. B.; Cai, J. R.; Yao, L. Q.; Lin, L. M.; Cai, L. P.; Chen, G. L. Sputtering of molybdenum as a promising back electrode candidate for superstrate structured Sb_2S_3 solar cells. *Adv. Sci.* **2023**, *10*, 2303414.

[19] Mathews, I.; Kantareddy, S. N.; Buonassisi, T.; Peters, I. M. Technology and market perspective for indoor photovoltaic cells. *Joule* **2019**, *3*, 1415–1426.

[20] Farhana, M. A.; Manjceevan, A.; Bandara, J. Recent advances and new research trends in Sb_2S_3 thin film based solar cells. *J. Sci.: Adv. Mater. Devices* **2023**, *8*, 100533.

[21] You, F. G.; Chen, S. W.; Ma, T. J.; Xiao, F.; Chen, C.; Hsu, H. Y.; Song, H. S.; Tang, J. Reactive ion etching activating TiO_2 substrate for planar heterojunction Sb_2S_3 solar cells with 6.06% efficiency. *Energy Technol.* **2022**, *10*, 2200940.

[22] Lin, W. W.; Guo, W. T.; Yao, L. Q.; Li, J. M.; Lin, L. M.; Zhang, J. M.; Chen, S. Y.; Chen, G. L. Zn(O,S) buffer layer for *in situ* hydrothermal Sb_2S_3 planar solar cells. *ACS Appl. Mater. Interfaces* **2021**, *13*, 45726–45735.

[23] Moshfeghi, E.; Entezari, M. H. Enhancement of the photovoltaic performance of perovskite solar cells via sono-synthesis of Al-doped TiO_2 as the electron transport layer. *Int. J. Energy Res.* **2022**, *46*, 23465–23479.

[24] Jagtap, C.; Kadam, V.; Jadkar, S.; Patole, S.; Pathan, H. Improvement in photovoltaic performance of dye-sensitized solar cell using ruthenium as dopant into titania. *J. Mater. Sci.: Mater. Electron.* **2023**, *34*, 1935.

[25] Nwankwo, U.; Nkele, A. C.; Arendse, C. J.; Ozoemena, K. I.; Ekwealor, A. B. C.; Jose, R.; Maaza, M.; Ezema, F. I. Effects of p-type-metal-doping (Ba, Cs, and Y) of the compact-TiO_2 electron transporting layer on the photovoltaic properties of n-i-p perovskite solar cells. *J. Mater. Sci.: Mater. Electron.* **2023**, *34*, 1891.

[26] Ishaq, M.; Chen, S.; Farooq, U.; Azam, M.; Deng, H.; Su, Z. H.; Zheng, Z. H.; Fan, P.; Song, H. S.; Liang, G. X. High open-circuit voltage in full-inorganic Sb_2S_3 solar cell via modified Zn-doped TiO_2 electron transport layer. *Solar RRL* **2020**, *4*, 2000551.

[27] Zeng, Y. Y.; Huang, J. L.; Li, J. J.; Sun, K. W.; Shah, U. A.; Deng, H.; Zhang, X. Y.; Sha, C. H.; Qian, C.; Song, H. S. et al. Comparative study of TiO_2 and CdS as the electron transport layer for Sb_2S_3 solar cells. *Solar RRL* **2022**, *6*, 2200435.

[28] Feng, M. J.; Zuo, C. T.; Xue, D. J.; Liu, X. H.; Ding, L. M. Wide-bandgap perovskites for indoor photovoltaics. *Sci. Bull.* **2021**, *66*, 2047–2049.

[29] Xie, L.; Song, W.; Ge, J. F.; Tang, B. C.; Zhang, X. L.; Wu, T.; Ge, Z. Y. Recent progress of organic photovoltaics for indoor energy harvesting. *Nano Energy* **2021**, *82*, 105770.

[30] Gao, H. H.; Li, J. Y.; Peng, X. Q.; Huang, Y. Q.; Zhao, Q.; Wang, H. L.; Wu, T.; Sheng, S. W.; Tang, R. F.; Chen, T. Band gap adjustable antimony selenosulfide indoor photovoltaics with 20% efficiency. *Solar RRL* **2024**, *8*, 2400389.

[31] Cao, R.; Lv, K.; Shi, C. W.; Wang, Y. Q.; Ye, C. S.; Guo, F. L.; Hu, G. J.; Chen, W. C. Efficient Sb_2S_3 and low Se content $Sb_2Se_yS_{3-y}$ indoor photovoltaics. *ACS Appl. Mater. Interfaces* **2024**, *16*, 42513–42521.

[32] Wang, L. B.; Cheng, B.; Zhang, L. Y.; Yu, J. G. *In situ* irradiated XPS investigation on S-scheme TiO_2@$ZnIn_2S_4$ photocatalyst for efficient photocatalytic CO_2 reduction. *Small* **2021**, *17*, 2103447.

[33] Torres-Ceron, D. A.; Amaya-Roncancio, S.; Riva, J. S.; Vargas-Eudor, A.; Escobar-Rincon, D.; Restrepo-Parra, E. Incorporation of P^{5+} and P^{3-} from phosphate precursor in TiO_2:P coatings produced by PEO: XPS and DFT study. *Surf. Coat. Technol.* **2021**, *421*, 127437.

[34] Lai, L.; Jin, S.; Hu, H. Z.; Wang, S. L.; Wu, C.; Wu, F. M.; Guo, D. Y. Modulation of bipolar ultraviolet current in TiO_2 nanofilms for switching logic devices via Ti valence state control. *ACS Appl. Nano Mater.* **2023**, *6*, 23557–23564.

[35] Guo, H. F.; Zhu, H.; Geng, K. J.; Zhang, T. Y.; Huang, S.; Yang, Y. S.; Fang, X.; Zhou, X. S.; Su, J.; Zhang, H. et al. Defect control for high efficiency antimony selenosulfide solar cells by interface engineering of buried monoatomic aluminum oxide layer. *Chem. Eng. J.* **2024**, *487*, 150499.

[36] Swami, S. K.; Kumar, N.; Radu, D. R.; Cho, S. W.; Lee, J. Lithium Incorporation into TiO_2 Photoanode for performance enhancement of dye-sensitized solar cells. *ACS Appl. Energy Mater.* **2023**, *6*, 8599–8606.

[37] Sun, Q. Z.; Shi, C.; Xie, W. H.; Li, Y. F.; Zhang, C. X.; Wu, J. H.; Zheng, Q.; Deng, H.; Cheng, S. Y. Defect synergistic regulations of Li&Na Co-doped flexible $Cu_2ZnSn(S,Se)_4$ solar cells achieving over 10% certified efficiency. *Adv. Sci.* **2023**, *11*, 2306740.

[38] Deng, H.; Feng, X. X.; Zhu, Q. Q.; Liu, Y. H.; Wang, G. D.; Zhang, C. X.; Zheng, Q.; Wu, J. H.; Wang, W. H.; Cheng, S. Y. 8.2%-efficiency hydrothermal Sb_2S_3 thin film solar cells by two-step RTP annealing strategy. *Sci. China Mater.* **2024**, *67*, 3666–3674.

[39] Zheng, J. Z.; Liu, C.; Zhang, L.; Chen, Y. J.; Bao, F. X.; Liu, J.; Zhu, H. B.; Shen, K.; Mai, Y. H. Enhanced hydrothermal heterogeneous deposition with surfactant additives for efficient Sb_2S_3 solar cells. *Chem. Eng. J.* **2022**, *446*, 136474.